Shaping the Profile and Dispersion of Waves Guided Between Spatiotemporally Dispersive, Electrically and Magnetically Conductive Metasurface Boundaries

Odysseas Tsilipakos, *Senior Member, IEEE*, and Thomas Koschny

***Abstract*—Metasurfaces have been utilized pervasively to manipulate the wavefront of structured beams propagating in free space. However, they also enable us to create nontrivial waveguide boundaries which offer novel opportunities for the manipulation of the mode profile and propagation constant of electromagnetic waves confined in the space enclosed by them. Here, we study a waveguide that is formed by a general class of metasurfaces which are both electrically and magnetically polarizable, support multiple resonances, and exhibit temporal and spatial dispersion. We investigate the opportunities offered by tailoring the temporal dispersion of the surface conductivities and study three different cases of spatial dispersion, namely, no dispersion, an ideal case of very specific dispersion of the form $\sigma_{se} \propto k_t$ and $\sigma_{sm} \propto 1/k_t$, and the realistic dispersion of an actual physical implementation based on a metal-backed cut-wire unit cell. Both analytical derivations and full wave numerical simulations are performed for addressing the different scenarios and verifying the results. We show that the proposed metasurface waveguides can enable (i) the ability to shape the mode profile from concave, to flat, to convex and (ii) the possibility of both superluminal and subluminal propagation, as well as both normal and anomalous group velocity dispersion. An example application of controlling the mode profile along propagation is showcased, highlighting the potential of metasurfaces as waveguide boundaries.**

***Index Terms*—Metasurfaces, waveguides, multiresonant boundaries, dispersion engineering, mode profile.**

I. Introduction

METASURFACES (MSs), thin artificial materials composed of sub-wavelength resonant meta-atoms, have been intensively investigated for a broad range of applications at frequencies ranging from microwaves to the visible [1], [2]. MSs have been mainly studied as free-space structures, enabling the control and shaping of plane waves and structured beams, including characteristics such as propagation direction, amplitude, polarization, and spectral composition.

MSs can also find great use in guided-wave structures. As early as 2009, metasurfaces comprised of resonant dielectric particles were considered as boundaries defining a parallel plate waveguide [3]. In the following years, parallel-plate and rectangular geometries [3]–[7], as well as circular closed geometries [8], [9] were further studied. A single planar metasurface can also support and control propagating surface states [10], whereas an interface between juxtaposed metasurfaces has been shown to support protected edge states [11]–[13]. Importantly, a distinct advantage provided by the discrete nature of metasurfaces is the ability to (locally) tailor their properties by modifying the meta-atom geometry or altering the material properties. This allows for tunable and/or spatially-modulated metasurface boundaries that can enable interesting applications, such as leaky-wave antennas [14], waveguide mode converters and polarization rotators [15], as well as slow-light structures [16].

From a physics standpoint, compared to conventional waveguide boundaries (a metallic wall or interface between dielectrics), a metasurface can provide great versatility in the reflection phase supplied by the boundary, covering the entire range between a perfect electric conductor (PEC, $\phi_r = \pi$) and a perfect (artificial) magnetic conductor (PMC, $\phi_r = 2\pi$). This freedom is enabled by the resonant nature of the meta-atoms comprising the boundary and can be also emulated by corrugated boundaries [6]. The possibility for extra reflection phase can have implications for, e.g., overcoming the minimum width requirements in waveguides; such topics have also been addressed with left-handed metamaterials [17]–[19] Additional flexibility in the available phase margin and the ability for unidirectional scattering is unlocked in the case of metasurface boundaries which are both electrically and magnetically conductive. In a very recent study, the dispersion relation of coupled surface states supported in parallel-plate waveguides made of such boundaries has been studied [20].

In this work, we consider the general case of metasurface boundaries that are both electrically and magnetically polarizable, can support multiple resonances, and exhibit temporal and spatial dispersion [Fig. 1(a),(b)]. Multiple resonances allow to attain a very wide reflection phase span (greatly exceeding 2π) and, importantly, to tailor the dispersion of the reflection phase [$\phi_r(\omega)$], into linear [21], [22] and quadratic [23] profiles, for example. Moreover, the concurrent electric and magnetic nature can be exploited to nullify transmission through the boundary by "antimatching" the electric and magnetic surface conductivities ($\sigma_{se} = 4/\sigma_{sm}$) [21],

Manuscript submitted January 2024. Work at Ames Laboratory was supported by the Department of Energy (Basic Energy Sciences, Division of Materials Sciences and Engineering) under Contract No. DE-AC02-07CH11358. Support by the Hellenic Foundation for Research and Innovation (H.F.R.I.) under the "2nd Call for H.F.R.I. Research Projects to support Post-doctoral Researchers" (Project Number: 916, PHOTOSURF). (*Corresponding author: Odysseas Tsilipakos*, email: otsilipakos@eie.gr)

O. Tsilipakos is with the Theoretical and Physical Chemistry Institute, National Hellenic Research Foundation, GR-11635 Athens, Greece

T. Koschny is with Ames Laboratory—U.S. DOE and Department of Physics and Astronomy, Iowa State University, Ames, Iowa 50011, USA.

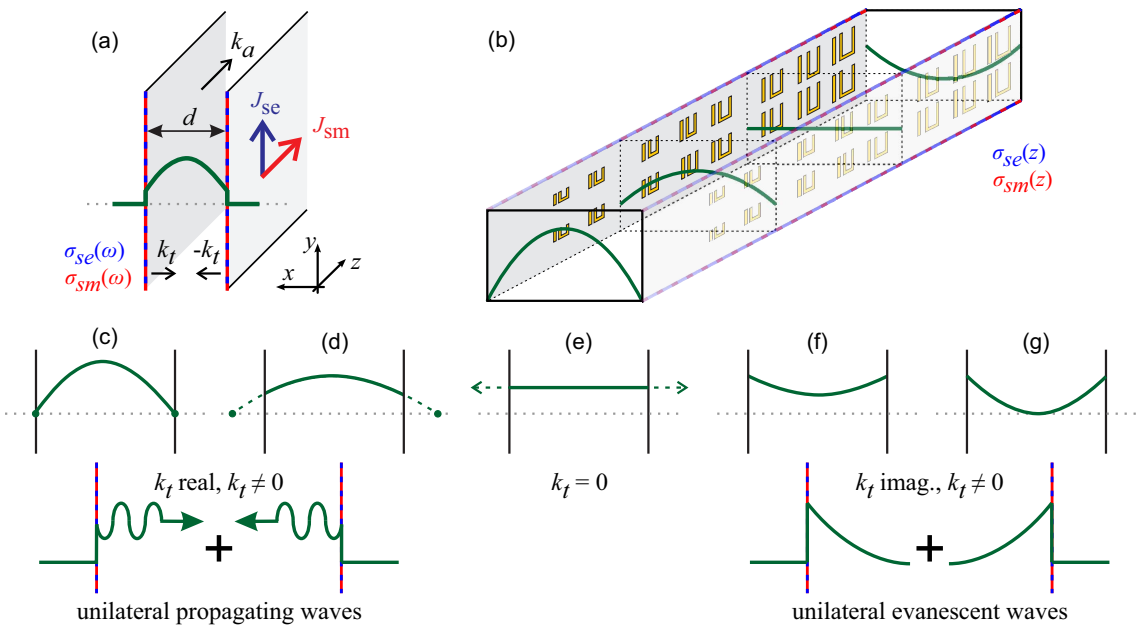

Fig. 1. (a) General problem statement: A waveguide is formed by impenetrable metasurface boundaries supporting electric and magnetic surface currents (J_{se} and J_{sm}), which are in general temporally and spatially dispersive. By tuning the complex surface conductivities of the boundaries, $\sigma_{se}(\omega)$ and $\sigma_{sm}(\omega)$, the mode profile and mode dispersion [axial wavevector or propagation constant, $k_a(\omega)$] can be controlled at will. (b) Rectangular waveguide with metasurface side-walls spatially modulated along the z-axis to exert control over the mode profile along propagation. (c-g) Different mode profiles enabled by the metasurface boundaries: "$\sin(x)$" profile (concave), flat profile, and "$\sinh(x)$" profile (convex). (d) Increasing the reflection phase provided by the boundaries above π (standard PEC reflection) can substitute for extra space, leads to a smaller transverse wavevector k_t, and stretches the mode profile, which is constructed by the superposition of two unilateral propagating waves (k_t predominantly real) along $\pm x$. (e) When $k_t = 0$, the mode profile becomes flat. (f,g) When k_t becomes predominantly imaginary, the interfering waves become evanescent (surface waves) and the mode profile changes curvature.

leading to impenetrable boundaries that confine the guided mode strictly within the waveguide. We are able to show modification of the waveguide mode profile from a sinusoidal form (integer multiples of half-wavelength, as is typical for a parallel-plate/rectangular waveguide) into a perfectly planar wavefront and all the way to coupled surface states, which exponentially decay away from the boundary [Fig. 1(c)-(g)]. Energy is guided through the volume of the waveguide in the first case, whereas it flows along the inside interfaces in the second one. These mode-profile regimes are accessed by obtaining a transverse wavevector (k_t) which is predominantly real [Fig. 1(c),(d)], zero [Fig. 1(e)], or predominantly imaginary [Fig. 1(f),(g)], respectively. Moreover, both superluminal ($k_a/k < 1$, where k_a is the axial wavevector or propagation constant) and subluminal ($k_a/k > 1$) propagation regimes are supported. Note that k_a is alternatively represented with β and k_a/k is the effective index of the waveguide mode, n_{eff}. Finally, both signs of the group velocity dispersion (β_2) are possible, leading to normal and anomalous dispersion regimes, which can be useful for dispersion compensation applications. The aforementioned theoretical findings are numerically demonstrated via full wave simulations of a practical printed-circuit-board (PCB) metasurface implementation targeted at microwave frequencies.

The rest of the paper is organized as follows. In Section II, the case of local (spatially-nondispersive) metasurface boundaries is considered. A transcendental equation that describes the dispersion of the supported modes is derived and verified by full wave simulations. Control over the mode profile and propagation constant are highlighted. Section III deals with metasurface boundaries that have a very specific form of spatial dispersion (nonlocality) and discusses the waveguiding characteristics that arise in this case. In Section IV, we consider a realistic case of spatial dispersion by studying an actual physical implementation of the metasurface boundary (cut-wire on a metal-backed dielectric substrate). Finally, Section V showcases an example application of controlling the mode profile along propagation via spatially-modulated (gradient) metasurface boundaries and Section VI is the concluding section.

II. Metasurface Boundaries with Local Conductivities

We will first focus on metasurfaces characterized by electric and magnetic conductivities, which are functions of ω (temporally dispersive) but not spatially dispersive (not explicitly dependent on k_a, or, equivalently, k_t). We are interested in calculating the dispersion of modes guided within a parallel plate waveguide formed by these metasurfaces, as illustrated in Fig. 1(a). We apply the boundary conditions for electric and magnetic fields. We focus on the TE polarization, for which $E_y = e_y(x)e^{ik_a z}$, $H_x = h_x(x)e^{ik_a z}$, and $H_z = h_z(x)e^{ik_a z}$ are the thee nonzero field components ($\exp[i(k_a z - \omega t)]$ dependence). Inside the waveguide ($0 \leq x \leq d$), the field

components are of the general form

$$h_z(x) = A\sin k_t x + B\cos k_t x, \tag{1a}$$

$$e_y(x) = \frac{-i\omega\mu}{k_t^2}\frac{\partial h_z}{\partial x} = \frac{-i\omega\mu}{k_t}(A\cos k_t x - B\sin k_t x), \tag{1b}$$

$$h_x(x) = \frac{ik_a}{k_t^2}\frac{\partial h_z}{\partial x} = \frac{ik_a}{k_t}(A\cos k_t x - B\sin k_t x), \tag{1c}$$

whereas outside the waveguide we prescribe zero fields, since the boundaries are assumed impenetrable by virtue of the "antimatching" condition, i.e., $\sigma_{se} = 4/\sigma_{sm}$ [21]. The boundary condition for the H-field at the $x = 0$ interface is

$$\hat{\mathbf{x}} \times (\mathbf{H}^{\text{in}} - \mathbf{H}^{\text{out}}) = \mathbf{J}_{se} = \sigma_{se}\frac{E_y^{\text{in}} + E_y^{\text{out}}}{2}\hat{\mathbf{y}}, \tag{2}$$

where $\hat{\mathbf{x}}$ and $\hat{\mathbf{y}}$ are unit vectors in the x and y directions, and yields $H_z = -(\sigma_{se}/2)E_y$. Note that because fields are discontinuous (i.e., they jump at the interfaces), for the constitutive relation of the electric surface current we have used the regularized *local* electric field, i.e., the average field on the two sides of the interface. Similarly, the boundary condition for the E-field at the $x = 0$ interface is

$$\hat{\mathbf{x}} \times (\mathbf{E}^{\text{in}} - \mathbf{E}^{\text{out}}) = -\mathbf{J}_{sm} = \sigma_{sm}\frac{H_z^{\text{in}} + H_z^{\text{out}}}{2}\hat{\mathbf{z}} \tag{3}$$

and yields $E_y = -(\sigma_{sm}/2)H_z$. Combining the two results we can indeed recover the antimatching condition $\sigma_{se} = 4/\sigma_{sm}$. Note that ultimately we need one boundary condition due to the interdependence (antimatching) between electric and magnetic surface conductivities. For the other boundary ($x = d$), the direction of the unit normal changes and we simply get $H_z = +(\sigma_{se}/2)E_y$ and $E_y = +(\sigma_{sm}/2)H_z$.

Applying the boundary condition at $x = 0$ and using (1) we find

$$B = \frac{i\omega\mu}{2k_t(\omega)}\sigma_{se}(\omega)A. \tag{4}$$

Subsequently, applying the boundary condition at $x = d$,

$$A\sin(k_t d) + B\cos(k_t d) = \sigma_{se}\frac{-i\omega\mu}{2k_t}[A\cos(k_t d) - B\sin(k_t d)] \tag{5}$$

and substituting (4), we can eliminate the coefficients A, B and arrive at the transcendental equation

$$\frac{2k_t}{i\omega\mu}\frac{1}{\sigma_{se}}\sin(k_t d) + 2\cos(k_t d) - \sigma_{se}\frac{i\omega\mu}{2k_t}\sin(k_t d) = 0, \tag{6}$$

which describes the dispersion of TE modes in the waveguide geometry of Fig. 1(a). Note that $\sigma_{se}(\omega)$ and $k_t(\omega)$ are functions of frequency with the dependence suppressed for brevity. For a given surface conductivity $\sigma_{se}(\omega)$ (note that the magnetic conductivity does not appear, since it is related with the electric one), one can solve for the transverse wavevector $k_t(\omega)$ and calculate the axial wavevector through $k^2 = k_a^2 + k_t^2$. The mode profile is then fully described by (1) and (4).

We note that TM modes are described by the same characteristic (transcendental) equation [equation (6)]. The field profile changes in this case with the nonzero field components being E_x, E_z, and H_y.

Equation (6) can also be cast in a more concise form in terms of the "effective" conductivities $\tilde{\sigma}_{se} = \zeta\sigma_{se}/2$ and $\tilde{\sigma}_{sm} = \sigma_{sm}/(2\zeta)$ ($\zeta^{\text{TE}} = \omega\mu/k_t$ for the TE polarization), which reads:

$$i\left(\tilde{\sigma}_{se} + \frac{1}{\tilde{\sigma}_{se}}\right)\sin(k_t d) - 2\cos(k_t d) = 0. \tag{7}$$

This form may prove useful since the effective conductivities are directly related with the plane-wave reflection/transmission scattering coefficients through

$$\tilde{\sigma}_{se} = \frac{\zeta\sigma_{se}}{2} = \frac{1 - r - t}{1 + r + t}, \tag{8a}$$

$$\tilde{\sigma}_{sm} = \frac{\sigma_{sm}}{2\zeta} = \frac{1 + r - t}{1 - r + t}, \tag{8b}$$

where ζ is the wave impedance which equals $\zeta^{\text{TE}}(\theta) = \omega\mu/k_\perp = \eta\sec(\theta)$ and $\zeta^{\text{TM}}(\theta) = k_\perp/(\omega\varepsilon) = \eta\cos(\theta)$ for the TE and TM polarization, respectively; θ is the incidence angle and $\eta = \sqrt{\mu/\varepsilon} = \sqrt{\mu_0\mu_r}/\sqrt{\varepsilon_0\varepsilon_r}$ is the characteristic impedance of the homogeneous host medium. For a derivation of (8) see Sec. S1 in the Supplementary Material, SM, document). Solving (8) for r, t we find

$$r = \frac{-\tilde{\sigma}_{se} + \tilde{\sigma}_{sm}}{1 + \tilde{\sigma}_{se}\tilde{\sigma}_{sm} + \tilde{\sigma}_{se} + \tilde{\sigma}_{sm}}, \tag{9a}$$

$$t = \frac{1 - \tilde{\sigma}_{se}\tilde{\sigma}_{sm}}{1 + \tilde{\sigma}_{se}\tilde{\sigma}_{sm} + \tilde{\sigma}_{se} + \tilde{\sigma}_{sm}}. \tag{9b}$$

Note, however, that the form of (7) hides the dependence of $\tilde{\sigma}_{se}$ on k_t, which is two-fold: via the physical conductivity σ_{se} and via the wave impedance ζ.

In realistic physical implementations of metasurfaces, the physical surface conductivity is in principle always spatially dispersive, i.e., a function of k_t, by virtue of discreteness and finite spacing of the meta-atoms. For deeply subwavelength MSs this is usually not pronounced. In addition, there are known approaches to suppress spatial dispersion. For example, in the case of metal-backed metasurfaces, which are most relevant to the physical implementation suggested in Section IV, mushroom-type unit cells have been shown to suppress spatial dispersion [24].

We now consider a specific example of spatially nondispersive (local) metasurface boundaries which are characterized by the conductivities depicted in Fig. 2(a). At the lowest frequency under study (kd/π=1), the electric conductivity is on resonance [$\text{Re}(\sigma_{se}) \to \infty$], translating into a PEC-style reflection. The real parts of the conductivities (correspond to dissipative loss) are plotted in the SM document, Fig. S1. It can be seen that the real part is maximized on resonance, i.e., where the imaginary parts shift from positive to negative values. The conductivities in Fig. 2(a) are clearly temporally dispersive and they have been specified on the basis of providing a spectrally-linear reflection phase profile of the form $\phi_r(\omega) = \Phi_0 + \Phi_1(\omega - \Omega)$, where Ω is a "center" frequency. More specifically, we assume a reflection coefficient of the form $r(\omega) = -r_0\exp[i\phi_r(\omega)]$ with a spectrally-constant reflection amplitude $0 < r_0 \leq 1$ as well as $t(\omega) = 0$ by virtue of antimatching and make use of (8) to specify the corresponding conductivities. Note that the minus sign in the definition of r means that ϕ_r is the reflection phase "in excess of π", which would correspond to a standard PEC-style reflection. Such a metasurface with a linear phase profile can

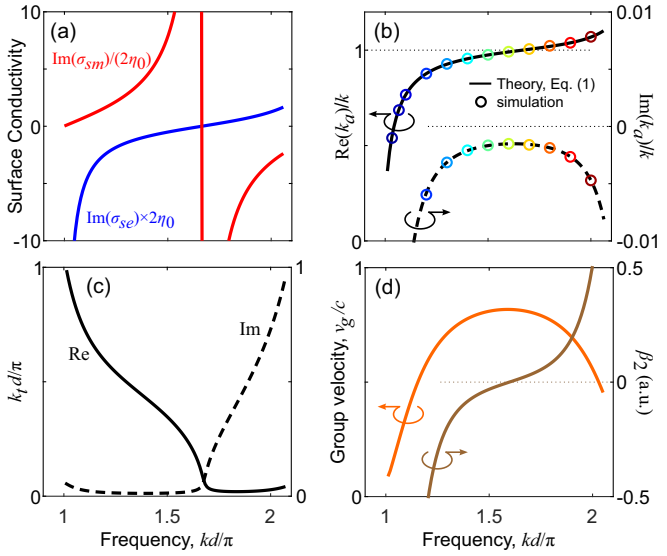

Fig. 2. Case of local (spatially nondispersive) metasurface boundaries. The boundaries are temporally-dispersive and designed so that for a specific incidence angle the reflection phase is linear with $\phi_r(\omega) = \Phi_0 + \Phi_1(\omega - \Omega)$, where $\Omega = \pi c/d$ (corresponds to $kd/\pi = 1$), $\Phi_0 = 0$, and $\Phi_1 = 0.75 \times 2\pi/\Omega$, and the reflection amplitude constant ($r_0 = 0.95$). (a) Dimensionless electric and magnetic surface conductivities (imaginary part). (b) Normalized axial wavevector (real and imaginary parts) for the TE_1 mode. At the frequency $kd/\pi = 1.67$, $\mathrm{Re}(k_a) = k$ and the mode profile flattens (see Fig. 3). Propagation loss ($|\,\mathrm{Im}\,k_a|$) is minimum there. The solution of the transcendental equation is verified by numerical eigenvalue simulations with COMSOL Multiphysics (solid markers). The color coding corresponds to the field profiles in Fig. 3. (c) Normalized transverse wavevector, real and imaginary parts. For frequencies below(above) $kd/\pi = 1.67$, k_t is predominantly real(imaginary) and the mode profile is constructed by unilateral propagating(evanescent) waves. (d) Group velocity and group velocity dispersion. Both anomalous ($\beta_2 < 0$) and normal ($\beta_2 > 0$) dispersion regimes are possible.

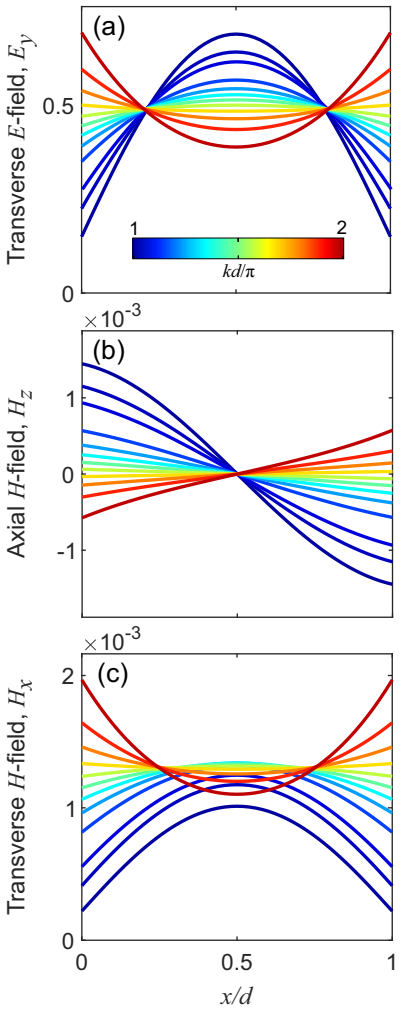

Fig. 3. Evolution of TE_1 mode profile with frequency in the range $kd/\pi \in (1, 2]$. The selected frequency points correspond to the markers in Fig. 2(b) and are color-coded accordingly. (a) Transverse E-field component, E_y. (b) Axial H-field component, H_z. (c) Transverse H-field component, H_x. At $kd/\pi = 1.67$, the transverse components become perfectly flat and the axial component zero. This corresponds to a "plane wave" albeit across a finite area. For frequencies $kd/\pi > 1.67$, the transverse components become convex (from concave) since they are constructed from unilateral evanescent waves (k_t predominantly imaginary).

be designed by spectrally interleaving electric and magnetic resonances [21] and has been experimentally demonstrated at microwave frequencies [22]. Note that the prescribed reflection coefficient holds for a single incidence angle: if the physical conductivity σ_{se} is independent of θ (local), then the effective conductivity $\tilde{\sigma}_{se}$, and consequently r, depend on θ through ζ, see (8).

Plugging the surface conductivity depicted in Fig. 2(a) in (6) we can solve for the supported modes. We focus on the lowest-order TE mode (TE_1) and plot the axial wavevector (real and imaginary parts) in Fig.2(b). The solution of the transcendental equation is verified by numerical eigenmode simulations with COMSOL Multiphysics (markers), where electric/magnetic surface current boundaries are prescribed via the surface conductivities depicted in Fig. 2(a). Interestingly, regions of both superluminal [$(\mathrm{Re}(k_a)/k < 1)$] and subluminal [$(\mathrm{Re}(k_a)/k > 1)$] propagation are found. At the frequency $kd/\pi = 1.67$, propagation loss ($|\,\mathrm{Im}\,k_a|$) is minimized and $\mathrm{Re}(k_a)/k$ becomes unity, marking the transition from superluminal to subluminal propagation. At the same frequency, the transverse wavevector switches from being predominantly real to predominantly imaginary [Fig. 2(c)]. This means that the mode profile switches from being constructed by a superposition of unilateral propagating waves (sine profile) to unilateral evanescent waves (hyperbolic sine profile), see Fig. 1 and equation (1).

To further support the above discussion we plot in Fig. 3 the TE_1 field profile, as calculated from the solutions of the transcendental equation. The curves correspond to the frequencies marked by the markers in Fig. 2(b), and are color-coded accordingly. All three nonzero components are plotted including the transverse E-field (E_y) [Fig. 3(a)], axial H-field (H_z) [Fig. 3(b)], and transverse H-field (H_x) [Fig. 3(c)]. Indeed, with increasing frequency the transverse components change from concave to convex [Fig. 3(a),(c)]. At $kd/\pi = 1.67$, they become perfectly flat, highlighting the analogy with a plane wave in free space (we have already remarked on $\mathrm{Re}(k_a)/k = 1$), albeit being nonzero only across a finite area. The axial component vanishes [Fig. 3(b)], indicating a transverse wave (as is the case for a plane wave).

Finally, in Fig. 2(d) we plot the group velocity and group velocity dispersion by taking the derivatives of the axial

wavevector with respect to frequency. Interestingly, regimes of both anomalous ($\beta_2 < 0$) and normal ($\beta_2 > 0$) dispersion are possible. This may be very useful for dispersion compensation applications without the need for coupling to a different waveguide or out-coupling to a free-space structure.

A different example of metasurface boundaries with local conductivities can by found in the SM document (Section S3). There, the prescription for the reflection phase is not linear but rather a dispersive profile corresponding to a singly-resonant metasurface with metal backing. The same qualitative features are observed.

III. Metasurface boundaries with specifically nonlocal conductivities

We now switch to a different idealized case and suppose that the surface conductivities of the metasurface are spatially dispersive (depend on k_t) but with a very specific dependence of the form $\sigma_{se} \propto k_t$ and $\sigma_{sm} \propto 1/k_t$ (note that this dependence does not disturb the antimatching condition). This means that the effective surface conductivities become *independent* of k_t [see equation (8)]. In effect, the reflection coefficient of the boundary (corresponds to the phase and amplitude modification of a plane-wave upon impinging on the metasurface) is also independent of k_t.

Suppose now that the metasurface boundary is designed to supply a reflection coefficient $r(\omega) = -r_0 \exp(i\phi_r) = -\exp(i\tilde{\phi}_r)$ with $\tilde{\phi}_r = \phi_r + i|\ln r_0|$, which is now valid for any k_t. Using (8), the corresponding effective surface conductivity is given by

$$\tilde{\sigma}_{se} = \frac{1 + e^{i\tilde{\phi}_r}}{1 - e^{i\tilde{\phi}_r}} = i\cot(\tilde{\phi}_r/2). \tag{10}$$

Substituting in (7) we find

$$-\left(\cot(\tilde{\phi}_r/2) - \frac{1}{\cot(\tilde{\phi}_r/2)}\right)\sin(k_t d) - 2\cos(k_t d) = 0. \tag{11}$$

Using the identity $\cot(2x) = (\cot^2 x - 1)/(2\cot x)$, (11) can be cast in the simple algebraic form

$$k_t d = m\pi - \tilde{\phi}_r, \tag{12}$$

where ϕ_r, and thus k_t, are functions of ω and m is the mode index. Equation (12) states that a standing wave (waveguide mode) is formed when a wave bouncing in the cross-section of the waveguide leads to constructive interference. When $\phi_r = 0$ we recover the standard cut-off condition for parallel-plate waveguides with metallic/PEC walls ($k_t d = m\pi$).

We now study a specific example with a linear reflection phase [$\phi_r(\omega) = \Phi_0 + \Phi_1(\omega - \Omega)$, where $\Omega = \pi c/d$ (corresponds to $kd/\pi = 1$), $\Phi_0 = 0$, and $\Phi_1 = 0.5 \times 2\pi/\Omega$] and spectrally-constant reflection amplitude ($r_0 = 0.95$). The reflection phase and amplitude as well as the corresponding effective surface conductivities are depicted in the SM document (Fig. S3). We consider the three lowest-order modes (TE_1, TE_2, and TE_3) and plot the corresponding axial wavevectors (real and imaginary parts) in Fig. 4(a). We can use directly (12) for this purpose, instead of solving the transcendental equation. The results have been verified with full wave simulations, which require an iterative procedure (updating the surface conductivities on the basis of the k_a value returned by the solver) to obtain a self-consistent solution. The cut-off frequencies for the three modes are normalized frequencies 1, 1.5, and 2, respectively ([Fig. 4(a)]. The evolution of the corresponding field profiles with frequency (transverse E-field component) are depicted Fig. 4(d), (e), and (f), respectively.

We next focus on the TE_1 mode, which becomes propagating at $kd/\pi = 1$. There, the reflection phase equals π and the field profile is of the form $\sin(\pi x/d)$, as in a standard metallic parallel-plate waveguide [Fig. 4(d)]. As the frequency increases, $\mathrm{Re}(k_a)/k$ approaches unity and the propagation loss ($|\mathrm{Im}\, k_a|$) decreases [Fig. 4(b)]. At frequency $kd/\pi = 2$, $\mathrm{Re}(k_a) = k$ and the mode profile becomes perfectly flat [see Fig. 4(d)]. This behavior is also imprinted on the transverse wavevector [Fig. 4(c)]. k_t inherits the linear dispersion of ϕ_r [cf. equation (12)] and decreases linearly until becoming zero for $kd/\pi = 2$. In contrast to the case studied in Section II (Fig. 2), for $kd/\pi > 2$ the transverse wavevector would become negative (not imaginary) and the TE_1 mode is no longer supported.

Since k_t inherits the dispersion of ϕ_r, if a spectrally-constant reflection phase is assumed, then k_t becomes independent of frequency and the same holds for the mode profile (see SM, Fig. S4). A degenerate case of this scenario is a conventional PEC boundary, where the reflection phase is π for all frequencies and the mode profile is fixed.

IV. Possible physical implementation of metasurface boundary: Realistic spatial dispersion

We proceed to study a realistic case of spatial dispersion, by considering an actual physical implementation of the metasurface boundary. The unit cell is depicted in Fig. 5(a). It consists of a cut-wire on a metal-backed dielectric substrate ($\varepsilon_r = 3.68$, $\tan\delta = 10^{-3}$). More specifically, a finite-length wire supporting an electric dipole resonance is periodically repeated in the yz-plane to create a resonant surface on the top metallization layer of a double-sided PCB circuit board. The dimensions are $w = 0.3$ mm, $L = 7$ mm, $a_z = 4$ mm, $a_y = 8$ mm, $t = 1.575$ mm, and the metallization thickness is 35 μm. The presence of the metal backplate allows for imparting magnetic polarizability in the bilayer structure and precludes transmission through the metasurface (impenetrable boundary).

We first study the metasurface as a free-space structure. By full wave simulations of the unit cell (periodic boundary conditions in the yz plane), we calculate the reflection coefficient for plane-wave scattering under oblique incidence (TE polarization, $\mathbf{E} = E_y\hat{\mathbf{y}}$). The reflection amplitude and reflection phase are depicted in Fig. 5(b) and (c), respectively, for incidence angles up to 85 deg. Evidently, the metasurface resonates at $\sim$8 GHz, with the position of the resonance shifting slightly towards lower frequencies with increasing incidence angle. A reflection dip appears on resonance [Fig. 5(b)]; it corresponds to increased absorption, since transmission is zero. Notice that

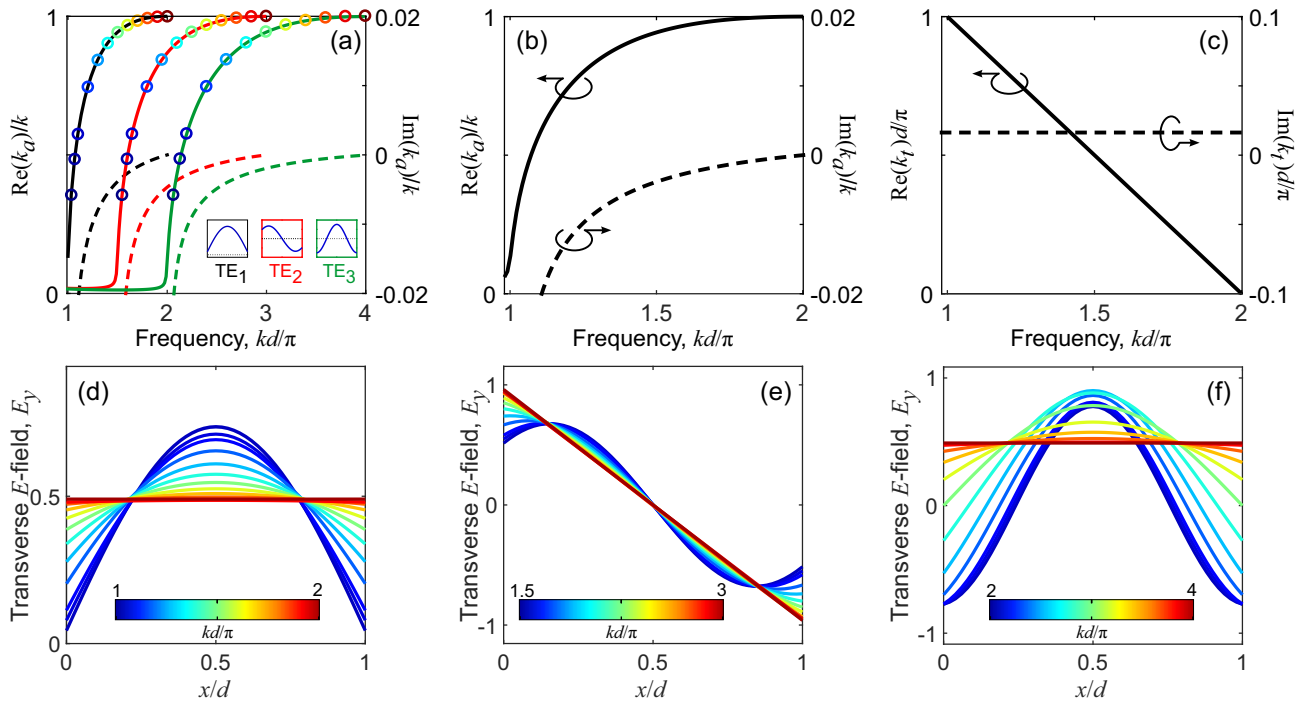

Fig. 4. Boundaries with nonlocal (spatially dispersive) conductivities with a very specific spatial dispersion so that the reflection phase provided by the metasurface boundary is independent of the incidence angle. The boundaries are temporally-dispersive and designed so that the reflection phase is linear $\phi_r(\omega) = \Phi_0 + \Phi_1(\omega - \Omega)$, where $\Omega = \pi c/d$ (corresponds to $kd/\pi = 1$), $\Phi_0 = 0$, and $\Phi_1 = 0.5 \times 2\pi/\Omega$ and the reflection amplitude constant $r_0 = 0.95$. (a) Dispersion of the three lowest-order TE modes in the normalized frequency range $kd/\pi = [1, 4]$. (b) Normalized axial wavevector (real and imaginary parts) for the TE$_1$ mode in the range $kd/\pi = [1, 2]$. At frequency $kd/\pi = 2$, $\mathrm{Re}(k_a) = k$ and the mode profile flattens [see panel (d)]. (c) Normalized transverse wavevector for the TE$_1$ mode, real and imaginary parts. As seen in (12), k_t inherits the linear dispersion of ϕ_r. In contrast to the case in Section II (Fig. 2), for $kd/\pi > 2$ the transverse wavevector would become negative (not imaginary). (d-f) Evolution of transverse E-field component for the TE$_1$ [panel (d)], TE$_2$ [panel (e)], and TE$_3$ [panel (f)] mode. The selected curves correspond to the frequency points denoted by the markers in panel (a) and are color-coded accordingly.

the reflection dip is shallow and $|r| > 0.9$ for all incidence angles considered. Associated with the resonance is a dispersive reflection phase profile of the form $\phi_r \propto 2\arctan[\gamma(\omega - \Omega)]$ [Fig. 5(c)], where a phase span of 2π is covered due to the concurrent electric and magnetic polarizability. The parameter γ measuring the steepness of the phase profile is associated with the resonance linewidth/quality factor [25] and changes with incidence angle. Clearly, sitting at a specific frequency both $|r|$ and ϕ_r change with incidence angle.

Instead of changing the operating frequency to scan the reflection phase, we can keep the operating frequency constant and scan the reflection phase by changing the resonant frequency of the meta-atom. This is demonstrated in Fig. 5(d),(e) where $f = 8$ GHz and the cut-wire length L varies from 6 to 7.9 mm. A wide range of reflection phases can be covered, reaching almost 2π for high incidence angles, where the supported resonance becomes sharper (radiation damping decreases). Note that if a larger phase span is required, we can tune more geometric parameters (e.g., wire width), modify the meta-atom geometry into more elaborate shapes, and/or use multiple meta-atoms inside the unit cell.

This unit cell is utilized to construct a parallel-plate waveguide [Fig. 6(a)]. The unit cell dimensions are as in the caption of Fig. 5 and the parallel plate distance is $d = 30$ mm (measured between the top metallization surfaces of the boundaries). The dispersion of the periodic waveguide is calculated by full wave eigenvalue simulations after specifying the phase advance along the propagation direction, $\Delta\varphi_z = k_a a_z$. Dispersion for two lowest-order TE modes is depicted in Fig. 6(b). The corresponding mode profiles (eigenvectors) are depicted in Fig. 6(c) and Fig. 6(d) for the TE$_1$ and TE$_2$ mode, respectively. They are evaluated at the center of the unit cell. Evidently, the TE$_1$ mode gradually acquires a flat profile ($\Delta\varphi_z \sim 40$ deg) and then acquires a convex curvature indicating the regime of imaginary k_t (superposition of evanescent waves). As the contributing surface states become more confined near each boundary they become weakly coupled. This explains the fact that the TE$_1$ and TE$_2$ modes become practically degenerate for $\Delta\varphi_z > 50$ deg. We should note that the field profiles in Fig. 6(c) can only approximate the case of abstract infinitesimally-thin boundaries depicted in Fig. 3(a). For instance, looking at the $\Delta\varphi_z = 40$ deg curve (purple) in Fig. 6(c), one sees that the profile stays flat for the largest extent of the waveguide cross-section, but drops to zero near the top metallization surface of each boundary. This is due to the fact that the curves are evaluated at the center of the unit cell where the cut-wire resides; the metallic material forces the transverse E-field to be zeroed out locally. Plotting the curves at a different position within the unit cell will produce a different behavior near the edges of the cross-section (see Fig. S5 of the SM document). In addition, there is naturally non-zero field inside the substrate of the metasurface

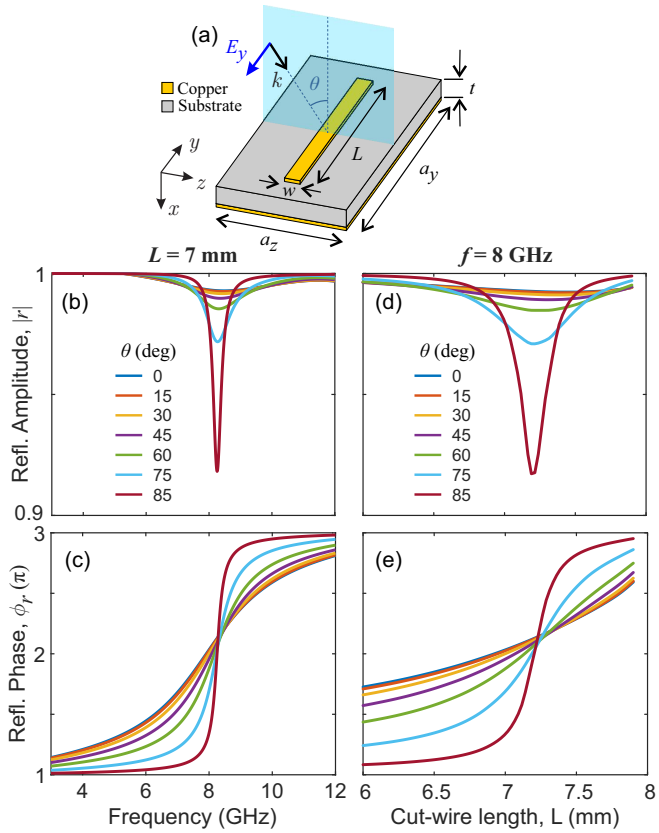

Fig. 5. (a) Metasurface unit cell composed of a cut-wire on a metal-backed dielectric substrate ($\varepsilon_r = 3.68$, $\tan\delta = 10^{-3}$). The dimensions are $w = 0.3$ mm, $L = 7$ mm, $a_z = 4$ mm, $a_y = 8$ mm, $t = 1.575$ mm, and the metallization thickness is 35 μm. (b,c) Plane-wave scattering from free-space periodic metasurface under oblique incidence (TE polarization), as calculated by full wave simulations. (b) Reflection amplitude as a function of frequency. A reflection dip appears on resonance (corresponds to absorption); notice that $|r| > 0.9$ for all incidence angles considered. (c) Reflection phase as a function of frequency. Evidently, both amplitude and phase depend on the incidence angle (as expected for a resonant metasurface), which translates into a spatially dispersive boundary for the waveguide studied in Fig. 6. (d,e) Plane-wave scattering at $f = 8$ GHz under oblique incidence (TE polarization), as the length L of the cut-wire varies. (d) Reflection amplitude and (e) reflection phase. A wide range of reflection phases can be covered, reaching almost 2π for high incidence angles where the supported resonance becomes sharper.

boundaries (gray strips).

Finally, in Fig. 6(e) we verify the full wave eigenvalue simulations by using the metasurface reflection data of Fig. 5 to reconstruct the dispersion curve of the TE_1 mode. Specifically, we first start from a guess value for the axial/tranverse wavevector, we then feed (12) with the corresponding reflection data and calculate a new value; more iterations follow until we reach a converged, self-consistent result. This way we are able to recover the part of the curve that corresponds to real k_t values (i.e., $\text{Re}(k_a)/k < 1$), for which we have reflection data available.

V. Applications: Waveguide with Gradient Walls for Mode Profile Modulation

To illustrate one possible application of the findings presented in this work we consider the scenario of a waveguide with spatially-modulated boundaries that can shape the mode profile along propagation. This concept was schematically illustrated in Fig. 1(b). Here, we consider a specific example where we start from standard metallic boundaries (π reflection phase) and progressively increase the supplied reflection phase up to 2.2π in order to push the TE_1 mode past the flat wavefront into the evanescent-wave regime (convex curvature) and then back [Fig. 7(a)]. We use full wave simulations with COMSOL Multiphysics considering abstract metasurface boundaries with local (spatially nondispersive) electric and magnetic surface conductivities. However, the required reflection phase can be supplied even by the rudimentary cut-wire unit cell in Section IV by simply using different cut-wire lengths and Fig. 5(e) as a look-up table. Note that in the ramp-up section, the effective index of the propagating wave starts from ~ 0.75 (region with PEC boundaries) and reaches unity at the point of flat wavefront. This translates into effective incidence angles on the metasurface boundaries ranging from ~ 50 to 90 degrees.

The field distribution (transverse E-field component) along the modulated waveguide is depicted in Fig. 7(b)-(d), illustrating the evolution of the mode profile. Notice the absence of a standing wave in the input section [Fig. 7(c)], indicating the absence of reflections. More specifically, we calculate $|S_{11}|^2 < 10^{-5}$. Transmission through the entire waveguide transition ($25\lambda_0$ long in total) is $|S_{21}|^2 = 0.84$ and $\sim 16\%$ of the injected power is lost in absorption (we have assumed $r_0 = 0.95$ when specifying the metasurface boundaries). Absorption is not negligible, especially at points where the electric field is maximum at the boundaries. Still, the transition efficiency is quite high for such a waveguide length. Since the "ramp-up" and "ramp-down" sections exhibit an adiabatic transition in the reflection phase of the boundaries (and their conductivity), reflections can only arise due to the discontinuities (kinks) between the five different sections (four kinks in total); however, is is seen that reflections from these discontinuities are negligible.

Next, we assume a more practical scenario where the "ramp-up/-down" sections are discretized in segments of length d_z and the resulting reflection phase profile is piecewise constant. Using a discretization of $d_z = \lambda_0/4$ results in 32 piecewise-constant segments along these sections, which are $8\lambda_0$ long (see Fig. S6 in the SM document). In this case, we calculate $|S_{11}|^2 = 9.3 \cdot 10^{-5}$ (return loss of -40 dB) and $|S_{21}|^2 \sim 0.84$. Even for $d_z = \lambda_0/2$ and $d_z = \lambda_0$, reflection is only $|S_{11}|^2 = 1.14 \cdot 10^{-4}$ and $|S_{11}|^2 = 1.36 \cdot 10^{-3}$, repspectively. The impedance mismatch between the different piecewise-constant segments remains negligible, resulting in minimal reflections.

Control over the mode profile can be useful to maximize/minimize interaction with inclusions within the waveguide or tailor end-fire radiation from an open waveguide end. Control over the mode profile is also associated with control over the mode dispersion. For instance, relying on the results in Fig. 2(d), the "$\sin(x)$ profile" segment corresponding to positive β_2 values can be used for dispersion compensation of the "$\sinh(x)$ profile" segment (negative β_2 values) and vice-versa.

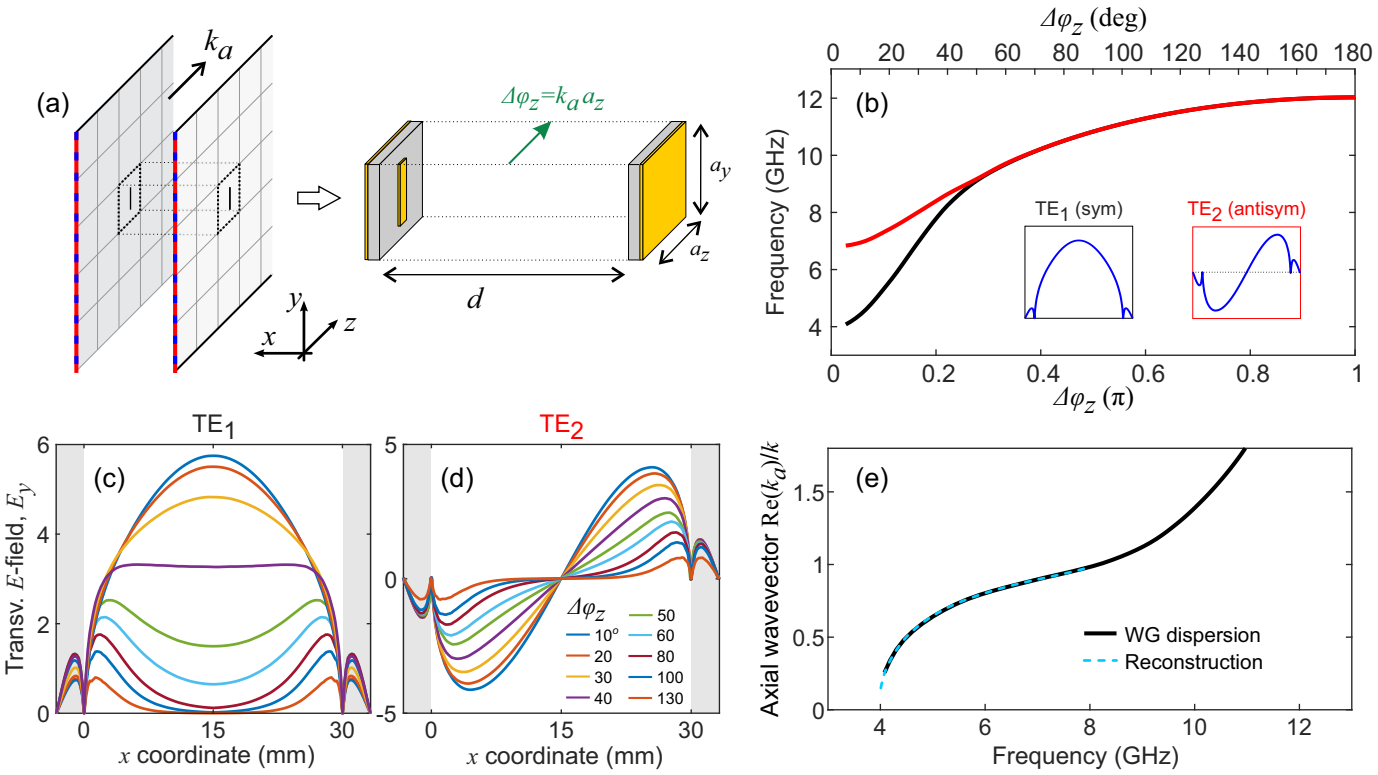

Fig. 6. (a) Periodic waveguide based on the unit cell of Fig. 5. The parallel plate distance is $d = 30$ mm. Waveguide dispersion is calculated by specifying $\Delta\varphi_z$ and solving an eigenvalue problem. (b) Dispersion of two lowest-order modes (TE$_1$ and TE$_2$). The modes become degenerate as the boundaries are progressively decoupled in the regime of contributing evanescent modes. (c) Mode profile evolution for the TE$_1$ mode. Notice the flat profile for $\Delta\varphi_z \sim 40$ deg and the gradual decoupling of the coupled surface waves for $\Delta\varphi_z > 50$ deg. (d) Mode profile evolution for the TE$_2$ mode. (e) Reconstruction of the first part of the waveguide dispersion (regime of contributing propagating modes) by using the plane-wave reflection data of Fig. 5.

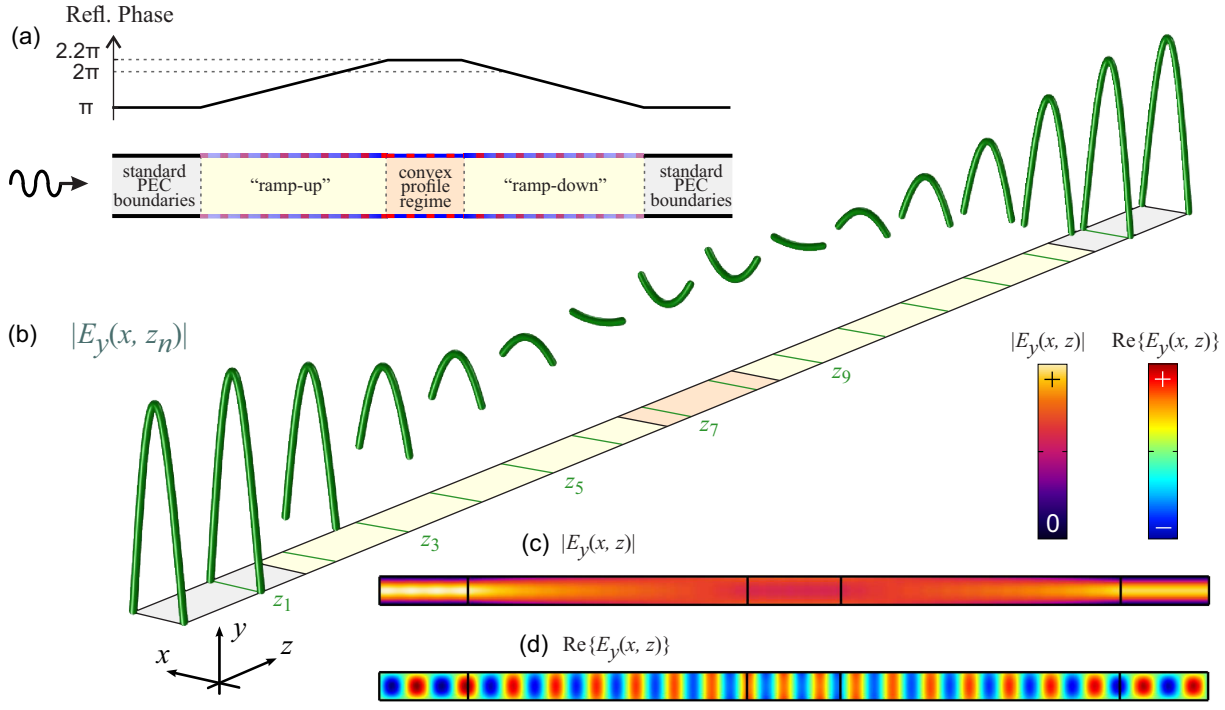

Fig. 7. Example of controlling the mode profile in a waveguide with gradient walls. (a) The surface conductivity is spatially modulated along the propagation direction (z), in order to progressively push the supported mode past the flat wavefront (corresponds to 2π reflection phase) and back. (b-d) Corresponding mode profile evolution along propagation as obtained from full wave simulations (COMSOL Multiphysics). (c) $|E_y(x, z)|$ field distribution. Notice the absence of reflections due to the adiabatic transition. (d) Real part of $E_y(x, z)$ component.

VI. Conclusion

In conclusion, we have proposed electrically and magnetically polarizable metasurfaces as waveguide boundaries. We have shown that they enable exciting opportunities, since (i) one can shape their temporal dispersion at will and (ii) the discrete nature of the metasurface allows to control their properties locally and produce gradient (spatially-modulated) boundaries. By analytical derivations and full wave simulations of a parallel-plate waveguide with metasurface boundaries, we have demonstrated (i) the ability to shape the mode profile from concave, to flat, to convex and (ii) the possibility of both superluminal and subluminal propagation, as well as both normal and anomalous dispersion. We have studied three different cases of spatial dispersion for the boundaries: no dispersion, an ideal case of specific dispersion, and the realistic dispersion of an actual physical implementation based on a metal-backed cut-wire unit cell. Finally, we have showcased an example of controlling the mode profile along propagation, highlighting the application potential of metasurfaces as waveguide boundaries.

Acknowledgments

Work at Ames Laboratory was supported by the Department of Energy (Basic Energy Sciences, Division of Materials Sciences and Engineering) under Contract No. DE-AC02-07CH11358. Support by the Hellenic Foundation for Research and Innovation (H.F.R.I.) under the "2nd Call for H.F.R.I. Research Projects to support Post-doctoral Researchers" (Project Number: 916, PHOTOSURF).

References

[1] S. B. Glybovski, S. A. Tretyakov, P. A. Belov, Y. S. Kivshar, and C. R. Simovski, "Metasurfaces: From microwaves to visible," *Physics Reports*, vol. 634, pp. 1–72, May 2016. [Online]. Available: https://doi.org/10.1016/j.physrep.2016.04.004

[2] D. C. Zografopoulos and O. Tsilipakos, "Recent advances in strongly resonant and gradient all-dielectric metasurfaces," *Materials Advances*, vol. 4, no. 1, pp. 11–34, 2023. [Online]. Available: https://doi.org/10.1039/d2ma00910b

[3] C. Holloway, E. Kuester, and D. Novotny, "Waveguides composed of metafilms/metasurfaces: The two-dimensional equivalent of metamaterials," *IEEE Antennas and Wireless Propagation Letters*, vol. 8, pp. 525–529, 2009. [Online]. Available: https://doi.org/10.1109/lawp.2009.2018123

[4] P. W. C. Hon, Z. Liu, T. Itoh, and B. S. Williams, "Leaky and bound modes in terahertz metasurfaces made of transmission-line metamaterials," *Journal of Applied Physics*, vol. 113, no. 3, Jan. 2013. [Online]. Available: https://doi.org/10.1063/1.4776761

[5] B. Byrne, N. Raveu, N. Capet, G. L. Fur, and L. Duchesne, "MODAL ANALYSIS OF RECTANGULAR WAVEGUIDES WITH 2d METAMATERIALS," *Progress In Electromagnetics Research C*, vol. 70, pp. 165–173, 2016. [Online]. Available: https://doi.org/10.2528/pierc16092904

[6] G. Valerio, Z. Sipus, A. Grbic, and O. Quevedo-Teruel, "Accurate equivalent-circuit descriptions of thin glide-symmetric corrugated metasurfaces," *IEEE Transactions on Antennas and Propagation*, vol. 65, no. 5, pp. 2695–2700, May 2017. [Online]. Available: https://doi.org/10.1109/tap.2017.2677923

[7] X. Ma, M. S. Mirmoosa, and S. A. Tretyakov, "Parallel-plate waveguides formed by penetrable metasurfaces," *IEEE Transactions on Antennas and Propagation*, vol. 68, no. 3, pp. 1773–1785, Mar. 2020. [Online]. Available: https://doi.org/10.1109/tap.2019.2934580

[8] N. Raveu, B. Byrne, L. Claudepierre, and N. Capet, "Modal theory for waveguides with anisotropic surface impedance boundaries," *IEEE Transactions on Microwave Theory and Techniques*, vol. 64, no. 4, pp. 1153–1162, Apr. 2016. [Online]. Available: https://doi.org/10.1109/tmtt.2016.2533387

[9] Z. H. Jiang, L. Kang, and D. H. Werner, "Conformal metasurface-coated dielectric waveguides for highly confined broadband optical activity with simultaneous low-visibility and reduced crosstalk," *Nature Communications*, vol. 8, no. 1, Aug. 2017. [Online]. Available: https://doi.org/10.1038/s41467-017-00391-0

[10] E. Martini, M. Mencagli, and S. Maci, "Metasurface transformation for surface wave control," *Philosophical Transactions of the Royal Society A: Mathematical, Physical and Engineering Sciences*, vol. 373, no. 2049, p. 20140355, Aug. 2015. [Online]. Available: https://doi.org/10.1098/rsta.2014.0355

[11] W.-J. Chen, Z.-Q. Zhang, J.-W. Dong, and C. T. Chan, "Symmetry-protected transport in a pseudospin-polarized waveguide," *Nature Communications*, vol. 6, no. 1, Sep. 2015. [Online]. Available: https://doi.org/10.1038/ncomms9183

[12] E. Martini, M. G. Silveirinha, and S. Maci, "Exact solution for the protected TEM edge mode in a PTD-symmetric parallel-plate waveguide," *IEEE Transactions on Antennas and Propagation*, vol. 67, no. 2, pp. 1035–1044, Feb. 2019. [Online]. Available: https://doi.org/10.1109/tap.2018.2880091

[13] A. Monti, S. Vellucci, M. Barbuto, D. Ramaccia, V. Verri, F. Vernì, C. Massagrande, A. Toscano, and F. Bilotti, "Line-wave waveguides: Design procedure and performance comparison," in *2023 17th European Conference on Antennas and Propagation (EuCAP)*, 2023, pp. 1–5.

[14] A. Ohadi and G. V. Eleftheriades, "Fixed-frequency beam-steering using slotted waveguide with tunable impedance walls," *IEEE Open Journal of Antennas and Propagation*, vol. 2, pp. 978–990, 2021. [Online]. Available: https://doi.org/10.1109/ojap.2021.3115342

[15] Z. Li, M.-H. Kim, C. Wang, Z. Han, S. Shrestha, A. C. Overvig, M. Lu, A. Stein, A. M. Agarwal, M. Lončar, and N. Yu, "Controlling propagation and coupling of waveguide modes using phase-gradient metasurfaces," *Nature Nanotechnology*, vol. 12, no. 7, pp. 675–683, Apr. 2017. [Online]. Available: https://doi.org/10.1038/nnano.2017.50

[16] Z. H. Fang, H. Chen, F. S. Yang, C. R. Luo, and X. P. Zhao, "Slowing down light using a dendritic cell cluster metasurface waveguide," *Scientific Reports*, vol. 6, no. 1, Nov. 2016. [Online]. Available: https://doi.org/10.1038/srep37856

[17] P. Tassin, X. Sahyoun, and I. Veretennicoff, "Miniaturization of photonic waveguides by the use of left-handed materials," *Applied Physics Letters*, vol. 92, no. 20, May 2008. [Online]. Available: https://doi.org/10.1063/1.2936299

[18] I. V. Shadrivov, A. A. Sukhorukov, and Y. S. Kivshar, "Guided modes in negative-refractive-index waveguides," *Physical Review E*, vol. 67, no. 5, May 2003. [Online]. Available: https://doi.org/10.1103/physreve.67.057602

[19] A. Alu and N. Engheta, "Guided modes in a waveguide filled with a pair of single-negative (SNG), double-negative (DNG), and/or double-positive (DPS) layers," *IEEE Transactions on Microwave Theory and Techniques*, vol. 52, no. 1, pp. 199–210, Jan. 2004. [Online]. Available: https://doi.org/10.1109/tmtt.2003.821274

[20] K. Hosseini, H. Younesiraad, and M. Dehmollaian, "Study of parallel-plate waveguides bordered by reactive huygens metasurfaces," *IEEE Transactions on Antennas and Propagation*, vol. 71, no. 4, pp. 3371–3381, Apr. 2023. [Online]. Available: https://doi.org/10.1109/tap.2023.3242454

[21] O. Tsilipakos, T. Koschny, and C. M. Soukoulis, "Antimatched electromagnetic metasurfaces for broadband arbitrary phase manipulation in reflection," *ACS Photon.*, vol. 5, no. 3, pp. 1101–1107, 2018.

[22] O. Tsilipakos, L. Zhang, M. Kafesaki, C. M. Soukoulis, and T. Koschny, "Experimental implementation of achromatic multiresonant metasurface for broadband pulse delay," *ACS Photon.*, vol. 8, no. 6, pp. 1649–1655, 2021.

[23] O. Tsilipakos and T. Koschny, "Multiresonant metasurfaces for arbitrarily broad bandwidth pulse chirping and dispersion compensation," *Phys. Rev. B*, vol. 107, p. 165408, Apr 2023. [Online]. Available: https://link.aps.org/doi/10.1103/PhysRevB.107.165408

[24] O. Luukkonen, M. Silveirinha, A. Yakovlev, C. Simovski, I. Nefedov, and S. Tretyakov, "Effects of spatial dispersion on reflection from mushroom-type artificial impedance surfaces," *IEEE Transactions on Microwave Theory and Techniques*, vol. 57, no. 11, p. 2692–2699, Nov. 2009. [Online]. Available: http://dx.doi.org/10.1109/TMTT.2009.2032458

[25] T. Christopoulos, O. Tsilipakos, G. Sinatkas, and E. E. Kriezis, "On the calculation of the quality factor in contemporary photonic resonant structures," *Optics Express*, vol. 27, no. 10, p. 14505, May 2019. [Online]. Available: https://doi.org/10.1364/oe.27.014505

Odysseas Tsilipakos (S'06-M'14-SM'19) obtained the diploma and PhD degrees from the Department of Electrical and Computer Engineering, Aristotle University of Thessaloniki (AUTh) in 2008 and 2013, respectively. From 2014 to 2015 he was a Postdoctoral Research Fellow with AUTh. From 2016 to 2022, he was a Postdoctoral Fellow with the Institute of Electronic Structure and Laser, Foundation for Research and Technology Hellas (IESL/FORTH). Since October 2022 he is serving as an elected Associate Researcher with the Theoretical and Physical Chemistry Institute, National Hellenic Research Foundation (TPCI/NHRF). His research interests include metasurfaces and metamaterials, plasmonics and nanophotonics, nonlinear optics in resonant and waveguiding structures, graphene and 2D photonic materials, and theoretical and computational electromagnetics. He is a (co-)author of ~ 60 refereed journal articles and ~ 80 international conference contributions. He is a Senior Member of IEEE and a member of The Optical Society (OSA).

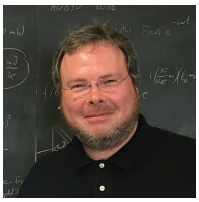

Thomas Koschny received his MS in Physics in 1997 and his PhD in Physics in 2001, both from the University of Leipzig, Germany. After postdoc positions at the Physikalisch-Technische Bundesanstalt (PTB) in Braunschweig, Germany, working on Quantum Hall systems, and the Institute of Electronic Structure and Lasers (IESL) at the Foundation for Research and Technology Hellas (FORTH) in Crete, Greece, he joined Costas Soukoulis' Metamaterials group at Ames Laboratory/Iowa State University in 2005. Since then he has been working across the fields of Light-Matter interaction, Electromagnetic wave propagation in complex materials, Metamaterials, Photonics, and Plasmonics from radio frequencies to daylight in Ames. Currently, he is a Scientist at Ameslab and Adjunct Associate Professor with the Department of Physics and Astronomy, ISU.